2D Electron thermal transport and electron thermal transport near magnetic islands

Beljaars, Koen P.

Award date:
2018

2D Electron thermal transport and electron thermal transport near magnetic islands

K.P. Beljaars

June 10, 2018

Contents

1 Introduction

Current day nuclear fusion reactors are designed for the confinement of a plasma at sufficiently high pressure to fuse deuterium and tritium with the goal of producing sustainable energy for the future. To maintain fusion reactions and produce net energy it is important to confine energy and plasma particles for a sufficient time under pressure. It is for this reason that tokamak reactors are built in a torus shape with a magnetic field of 2-5T in the toroidal direction such that the plasma ions and electrons are guided into making an infinite loop inside the reactor. However, a toroidal magnetic field created by coils wrapped around a vacuum vessel has a gradient in the radial direction and a magnetic field curvature. These two properties result into a drift of the electrons and ions in the plasma, which leads to a loss of confinement. To counter these drifts a current is driven in the toroidal direction by applying a voltage over the plasma. This current creates a poloidal magnetic field perpendicular to the toroidal magnetic field. In a simple torus with a circular cross section the combination of a toroidal and poloidal magnetic field creates magnetic field lines confined to surfaces that are shaped like a torus. These surfaces are called flux surfaces as the magnetic flux is contained in these surfaces. On the flux surfaces temperature and particle density are constant as particle and heat transport is much faster along the magnetic field lines than perpendicular to the magnetic field lines. The magnetic topology consisting of the poloidal and toroidal field together creates an equilibrium containing plasma particles and energy. Through collisions with particles gyrating around neighboring magnetic field lines however, energy still leaks out of the plasma. This creates one of the challenges of nuclear fusion research. Namely, understanding the thermal transport to find conditions under which energy loss from the plasma is minimal. This challenge can be quantified as striving for the highest energy confinement time τ_E. Which is defined as:

$$\tau_E = W/P_{loss}. \tag{1}$$

Where W is the total energy confined in the plasma and P_{loss} is the power loss from the plasma. The power loss of the plasma can increase when magnetic perturbations cause the magnetic field to reorganize and create what is known as a magnetic island. In a 2D cross section of the magnetic field lines, magnetic islands appear as nested flux surfaces separated from the bulk plasma as can be seen in figure (1). Magnetic islands have 2 regions of particular interest. The O-point in the middle where the magnetic field consists of concentric flux surfaces. And the X-point where the magnetic field is more chaotic and field line reconnection takes place. In 3D, the magnetic islands are shaped like tubes within the nested flux surfaces. These tubes go around toroidally and poloidally and close on themselves. The ratio of toroidal turns over poloidal (m/n) turns before closing on themselves is used to name and differentiate between magnetic islands as it is unique for their location in the plasma. Figure (2) shows a 3D representation of a $m/n = 2/1$ magnetic island from a simulation of the DIII-D tokamak published by the U.S.A. department of energy [1].

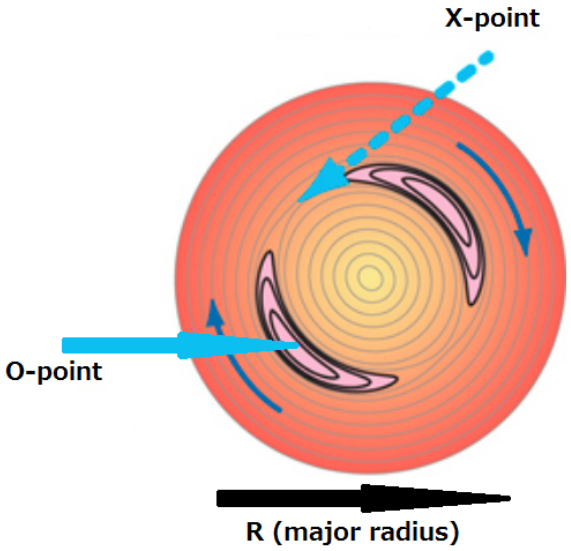

Figure 1: A sketch of the magnetic topology of a magnetic island (purple) in a tokamak with a cylindrical cross section. The light blue arrows indicate the location of the so called X-point and O-point areas of the magnetic island. The dark blue arrows indicate the rotation of the magnetic island in the poloidal direction over time.

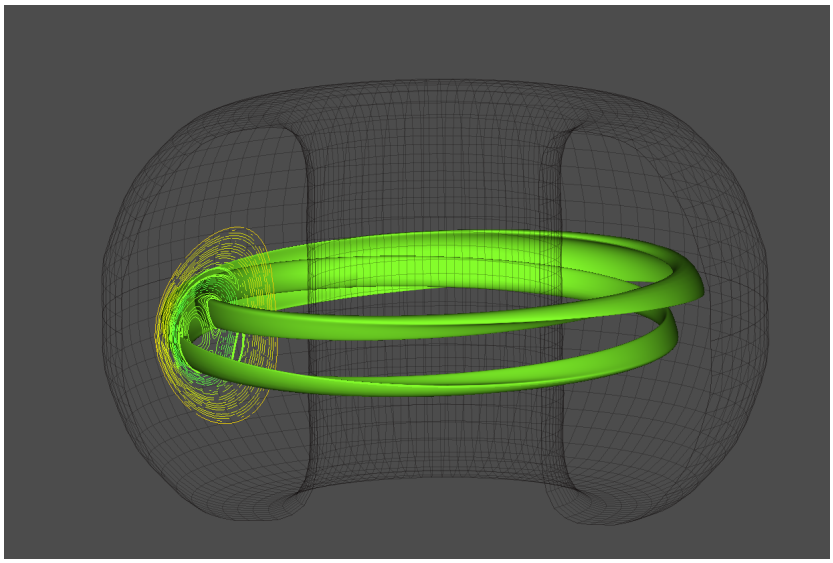

Figure 2: A simulation indicating the shape of a m/n = 2/1 magnetic island in the DIII-D reactor in green. The black grid indicates the vacuum vessel of the reactor and the yellow lines show a 2D cross section of the magnetic flux surfaces. Note how the magnetic island closes on itself after 2 laps around the length of the torus. This simulation has been done by S.Kruger using the NIMROD code. Published online by the USA department of energy [1].

1.1 Magnetic islands and electron thermal transport

In general magnetic islands are known for their ability to reduce the confinement time by enhancing the power loss from the plasma. The increase in power lost is caused by rapid transport of energy over the width of the island by fast transport over its outermost flux surfaces. Essentially causing a thermal shortcut over the width of the island. If the island is wide enough this can even lead to a disruption of the plasma. It has however been observed in multiple experiments that magnetic islands can also cause increased electron temperature gradients on the side towards the center of the plasma, suggesting thermal transport barrier behavior [2][3][4]. In a paper by M.J. Choi [2] it has been shown that magnetic islands have areas with varying degrees of electrostatic turbulence and poloidal flow on the inboard side. Specifically, that near the X-point exists a region with stronger turbulence and a weaker poloidal flow and on the inboard side from the O-point there is a region with less turbulence and stronger poloidal flow. It is then suggested that the strong poloidal flow near the O-point causes shear to disrupt turbulent currents which causes lowered flux surface averaged turbulent transport. This would then lead to the observed increased electron temperature gradient on the inboard side. This work will aim to test this hypothesis by measuring the electron thermal transport near the magnetic island in 2D.

1.2 Objective of this thesis

To test the hypothesis that the presence of a magnetic island can decrease the electron thermal transport on the inboard side this thesis will ask two research questions:

- Can a 1D diffusive heat transport model describe a 2D measurement of the thermal transport in a tokamak?
- Can lowered electron thermal transport be observed on the inboard side of a magnetic island lower compared to the unperturbed section of the tokamak plasma?

The physical quantity that will be used to examine these questions is the thermal diffusion coefficient χ that relates the heat flux q with the temperature gradient ∇T through:

$$q = -\chi \nabla T. \tag{2}$$

Also known as Fourier's law. With a constant heat flux, a high χ represents higher thermal transport and low temperature gradient and a lower χ represents lower thermal transport and a higher temperature gradient. To find the heat diffusion coefficient in the area near a magnetic island each section will answer a subquestion to leading up to answering the research questions in section 6 and 7.

- How does one calculate the heat diffusion coefficient χ from the heat flux and temperature? Treated in section 2.
- How does one measure the temperature in a tokamak in 2D? Treated in section 3.

- On what basis are transport differences expected to occur near a magnetic island? Treated in section 4.
- How does one analyze a temperature measurement? And how does the error on the temperature measurements behave? Treated in section 5.

1.3 Approach to determining the electron heat transport near a magnetic island

To study heat transport in 2D and around a magnetic island in a controlled environment this experiment will make use of of the resonant magnetic perturbation (RMP) field of KSTAR to induce stationary magnetic islands in a plasma. The thermal transport coefficients will then be determined by means of a modulated heating experiment similar to work done by G. Spakman at TEXTOR [5] and work by S. Inagaki at LHD [6]. Modulated electron cyclotron resonance heating (MECRH) will be deposited off center such that the resulting heat wave travels outwards across the magnetic island. The propagation of this heat pulse will be imaged by 3 2D electron cyclotron emission imaging (ECEI) systems. A method is developed using a transformation of time dependent data to the frequency domain to arrive at an approximation of the electron heat diffusion coefficient. Section 2 will explicate the relation between the heat wave properties and the thermal diffusion coefficient by using a heat transport model based on cylindric geometry. Furthermore it will explain the role of a magnetic island related to the thermal transport as found in experiments.

2 Thermal transport in tokamaks

In a fully ionized plasma such as in a tokamak all transport mechanisms, be it of particles or energy, are based on collisions. The main component of the velocity of electrons and ions in a tokamak plasma is in the direction of the magnetic field lines due to the interaction of moving charged particles and magnetic fields. This means that transport inside a flux surface is orders of magnitude higher than perpendicular to the flux surface. Because of this property both density and temperature are constant on a flux surface and are therefore also called flux functions. In a classical cylindrical approximation of the plasma, transport across flux surfaces happens only due to the cyclotron rotation that every charged particle makes around a magnetic field line. By colliding with a particle circling a different field line on a nearby flux surface, energy gets transfered. In reality however the classical picture has been shown to predict values of energy transfer orders of magnitude lower than observed. The differences are attributed to a combination of geometric effects and electrostatic turbulence. On a coarser scale than single particle collisions the thermal transport can be represented by χ as the diffusional heat transport coefficient. This work makes use of thermal transport models previously derived in nuclear fusion literature. The main equations for these models can be found in the works of N. Lopes Cardozo [7], A. Jacchia [8] and M. van Berkel [9]. The work of M. van Berkel [9] also contains a summary of multiple approximations for the thermal diffusion coefficient and their accuracy. The following subsections will address the main equations and assumptions necessary to derive an equation for the electron heat diffusion coefficient and how magnetic islands relate to the thermal transport.

2.1 Electron heat diffusion coefficient approximations for tokamaks

The energy of electrons in a volume element is described by:

$$\frac{\partial}{\partial t}\left(\frac{3}{2}n_e T_e\right) = -\nabla \bullet \vec{q} + S_h. \tag{3}$$

Where q represents the heat flux, S_h the power of the heating sources injected into the plasma per volume element, n_e the electron density and T_e the electron temperature. The left hand of the equation describes the total energy contained in a plasma per volume element per unit time and the right hand is the energy transport through conduction and energy gain by heating. If the energy transport is assumed to be purely diffusional, the classical Fourier's law for the heat flux can be used:

$$\vec{q} = -n_e \chi \nabla T_e. \tag{4}$$

Where χ represents the heat diffusion coefficient. In this equation the heat diffusion coefficient has an important role as a variable by connecting a certain heat flux to a gradient of the temperature. Because for the upcoming experiments the plasma will be heated with a modulated heating source the temperature fluctuations will be dominant over density fluctuations which means the density on the left hand of the equation can be moved outside the derivative. This means the density can be divided away from each side of the equation. To indicate the change from a static temperature profile to temperature perturbations. the

temperature will be noted as $\tilde{T}$. It will also be assumed that measurements are not done at the deposition location of the heating so that $S_h = 0$. Which should be and accurate assumption as the applied heating will be localized and outside the measurement volume in the experiments. At the same time the plasma will be assumed to be cylindrical because of the high ratio of R/a (major radius by minor radius). In this cylindrical geometry the heat transport is only in the radial direction, thus simplifying equation (3) to:

$$\frac{3}{2}\frac{\partial \tilde{T}}{\partial t} = \frac{1}{\rho}\frac{\partial}{\partial \rho}\left(\rho\chi\frac{\partial \tilde{T}}{\partial \rho}\right). \tag{5}$$

Where ρ is the minor radius. The next step to finding a solution for χ is to transform the equation to the Fourier domain resulting into the following ordinary differential equation:

$$\frac{1}{\rho}\frac{\partial}{\partial \rho}\left(\rho\chi\frac{\partial \Theta}{\partial \rho}\right) - \frac{3}{2}i\omega\Theta = 0. \tag{6}$$

Where $\Theta(\rho, \omega)$ is the Fourier transform of the temperature, $i = \sqrt{-1}$ and ω is the angular frequency. This second order ordinary differential equation has an exact solution consisting of the modified Bessel functions of the first I_ν and second kind K_ν of order ν. Making the solution for the Fourier transform of T:

$$\Theta(\rho, \omega) = C_1(i\omega)K_0\left(\sqrt{\frac{3}{2}\frac{i\omega}{\chi}}\rho\right) + C_2(i\omega)I_0\left(\sqrt{\frac{3}{2}\frac{i\omega}{\chi}}\rho\right). \tag{7}$$

C_1 and C_2 represent the constants that depend on the boundary conditions. To continue the derivation it is necessary to say something about these constants. Because tokamak nuclear fusion reactors lose heat to the wall, temperature decreases in the radial direction, one can therefore assume that far from where measurements will be done the temperature converges to zero meaning $\lim_{\rho\to\infty}\Theta(\rho, \omega) = 0$. This means that $C_2 = 0$ as I_0 does not converge to 0 but to infinity for this limit. The next step is to take the logarithmic derivative to ρ to eliminate the need to find a value for C_1. The logarithmic derivative In this case results in:

$$\frac{\Theta'}{\Theta} = -\sqrt{\frac{3}{2}\frac{i\omega}{\chi}}\frac{K_1\left(\sqrt{\frac{3}{2}\frac{i\omega}{\chi}}\rho\right)}{K_0\left(\sqrt{\frac{3}{2}\frac{i\omega}{\chi}}\rho\right)}. \tag{8}$$

Here the prime denotes a derivative of Θ to ρ. The fraction of the two modified Bessel functions can be written as an infinite fraction which can be truncated to its shortest form as the following equation.

$$\frac{\Theta'}{\Theta} = -\sqrt{\frac{3}{2}\frac{i\omega}{\chi}}\left(1 + \frac{1}{-2\cdot\sqrt{\frac{3}{2}\frac{i\omega}{\chi}}\rho}\right). \tag{9}$$

For the perturbation experiment a heat pulse with a constant frequency will be injected so the left hand side of (9) can also be written as a single frequency

component $\Theta(\omega_0) = A \cdot e^{(i\phi)}$. Substituting this and its derivative to ρ and rewriting the equation one gets:

$$\sqrt{\frac{3}{2}\frac{i\omega_0}{\chi}} = -\left(\frac{A'}{A} + i\phi' + \frac{1}{2\rho}\right). \tag{10}$$

Squaring this equation and splitting it up in the real and imaginary part allows the derivation of two equations which can be combined to result in two approximations for χ. One equation containing the amplitude and the phase and one equation requiring only the phase.

$$\chi_1 = \frac{3}{4}\frac{\omega_0}{\phi'^2}, \tag{11}$$

$$\chi_2 = \frac{3}{4}\frac{\omega_0}{\phi'\left(\frac{A'}{A} + \frac{1}{2\rho}\right)} \tag{12}$$

These two approximations for the heat diffusion coefficient can be used in all further sections.

2.2 Thermal transport and Magnetic islands

Magnetic islands can be found in a plasma where a perturbation of the magnetic field, either through instabilities or induced by coils, influences a resonant magnetic flux surface by using free energy energy at the resonance to reconnect magnetic field lines. There is only a limited number of resonant flux surfaces, know as rational surfaces. Rational surfaces are flux surfaces in the magnetic field geometry that have field lines that close upon themselves with the ratio of toroidal divided by poloidal turns being a rational number. As each ratio uniquely defines the shape of the magnetic island that can appear at that surface, they are indicated by the notation m/n. Where m indicates the number of toroidal turns and n the number of poloidal turns before the magnetic island closes on itself. After being created a magnetic island will typically either grow or shrink. The rate at which this happens is known to depend on the current density inside the magnetic island. This means that driving a current in the one direction inside a magnetic island will shrink them away and driving a current in the other direction will cause them to grow.

Due to the idea that magnetic islands can only decrease the energy confinement time, most research has been focused on shrinking them. The relation between a magnetic island and the energy transport around it has however been found to be more complex, meaning it can either enhance or inhibit thermal transport [2][3][4]. Magnetic islands influence both the transport near their position and the energy contents of the entire plasma. Inside the magnetic islands the two regions around the X-point and O-point behave quite differently related to thermal transport. The O-point region acts essentially as a region of nested flux surfaces just like a tokamak with an unperturbed magnetic field. With the difference that these flux surfaces are a helical tube an have a cross section more akin to an elongated ellipse (see again in figure 1 and 2). Due to this structure the magnetic island guides the energy very quickly along the outer flux surface. As there is generally no heat deposited within a magnetic island this means the

temperature tends to flatten out within the O-point region. The X-point region does not have a constant structure due to the reconnection of field lines that takes place there and is therefore a region with fluctuating transport. Outside the separatrix of the magnetic island the plasma also behaves differently compared to an unperturbed plasma. On the basis of the behavior explained later in section 4 this leads to the second research question of this thesis.

2.3 Summary

This section explained the heat transport in a tokamak. The energy balance differential equation is used to derive three equations for the heat diffusion coefficient assuming a cylindric geometry and purely radial heat transport for a single harmonic component of a temperature perturbation. The ratio of the modified Bessel functions in equation 8 is truncated in its shortest form but can be expanded to contain more components of the infinite fraction for a more accurate approximation of χ. The influence of a magnetic island on the heat transport in its proximity and the transport inside the magnetic island are also discussed. In the upcoming experiments it will be assumed that the equations for χ derived for a cylindric geometry are still valid near the magnetic island as the magnetic field still consists of nested flux surfaces in this region. With the conditions and an equation for the heat diffusion coefficient known the next section will describe the method for detecting temperature modulations locally in two dimensions in a tokamak plasma.

3 Detection of 2D temperature profiles in a tokamak plasma

To be able to detect the amplitude, phase of a temperature modulation and their derivatives in a tokamak one can look at the rotating movement of the plasma particles in the magnetic field. During this movement the plasma ions and electrons emit electromagnetic waves with the same frequency as their rotation. The intensity of these waves is directly related to the temperature of the plasma particles. Subsections 3.1 and 3.2 will explain these properties and section 3.3 will argue for the detection of electron cyclotron radiation over ion cyclotron radiation and explain the method for making 2D images of electron temperature. Subsection 3.4 explains the KSTAR reactor where the experiments will be done and subsection 3.5 will explicate the KSTAR cyclotron radiation detection system.

3.1 Cyclotron radiation

To simplify the calculation showing the origin and properties of cyclotron radiation the assumption will be made that no electric fields are present and a plasma particle is only influenced by a magnetic field as in the reactor the electric field is only present to accelerate the particles in a direction and plays only a small role in the case of drifts. The cyclotron resonance equation is shown for the case of an electron. An explanation for the choice of electron radiation will be given in subsection 3.3. The difference between electrons and ions in these equations is only in the different mass and opposite charge. When the magnetic field is the only field interacting with an electron the equation of motion is given by:

$$\frac{d}{dt}(\gamma m_{e,0}\mathbf{v}) = -e(\mathbf{v} \times \mathbf{B}_0). \tag{13}$$

With γ being the relativistic factor, $m_{e,0}$ the electron rest mass, $\mathbf{v}$ the velocity vector and $\mathbf{B}_0$ the magnetic field vector. If a direction for the magnetic field is chosen along the Cartesian z-axis, the equations for the position and the velocity can be derived from (13). This derivation is skipped here as it is quite extensive and the only important result for this experiment is the cyclotron resonance frequencies. A full derivation and the source for this work can be found in [10]. The equation for the cyclotron radiation resonances becomes:

$$\omega_{r(m)} = \frac{m\Omega(1-\beta^2)^{1/2}}{1-\beta_{\|}\cos(\theta)}. \tag{14}$$

Where $\Omega = eB/m_{e,0}$ is called the cyclotron frequency and β is the ratio of the velocity of the electron v over the speed of light c. The factor m is a real integer indicating the discretization of frequency harmonics. From this equation a couple of things can be deduced. Firstly, the cyclotron frequency is only dependent on the magnetic field and the mass of the particle. Secondly, two broadening mechanisms are included in the resonance frequencies equation. The relativistic broadening $\gamma^{-1} = (1-\beta^2)^{1/2}$ caused by mass increase when particles move near the speed of light. And the Doppler broadening $1-\beta_{\|}\cos(\theta)$ caused by the emission of waves during movement relative to an observer dependent on

the observation angle between the line of sight and the electron velocity vector. In the case of electron velocities much smaller than the speed of light and perpendicular observation these factors however reduce to 1. The thermal electrons in a tokamak move at speeds that are mere percents of the speed of light and as such the factor β^2 can be neglected. Concerning the Doppler broadening the experiment is done under perpendicular observation Which means the second broadening term is also insignificant. This means that the mass and the magnetic field are the main factors that determine the cyclotron radiation frequency for the experiments. The frequency of radiation is now known but just as important is the propagation of this radiation through the plasma.

3.2 Black body radiation and wave propagation

The next equations describe the radiation propagation through the plasma for electron cyclotron waves. The transport over a 1D ray of light can be summarized with the equation from [10]:

$$\frac{\mathrm{d}I}{\mathrm{d}s} = j(\nu) - I\alpha(\nu). \tag{15}$$

With I the intensity of radiation, $\alpha(\nu)$ the absorption coefficient, s the distance of propagation and $j(\nu)$ the emissivity of the 1D volume with ν indicating the radiation frequency in Hz. This equation has the solution:

$$I(s_2) = I(s_1)\mathrm{e}^{(\tau_1-\tau_2)} + \int_{s_1}^{s_2} j(\nu)\mathrm{e}^{(\tau-\tau_2)}\mathrm{d}s. \tag{16}$$

through a length of medium from s_1 to s_2. With

$$\tau = \int^{s} \alpha(\nu)\mathrm{d}s. \tag{17}$$

The second term on the right hand can be rewritten assuming that j/α is uniform.

$$I(s_2) = I(s_1)\mathrm{e}^{(\tau_1-\tau_2)} + \int_{\tau_1}^{\tau_2} (j/\alpha)\mathrm{e}^{(\tau-\tau_2)}\mathrm{d}\tau. \tag{18}$$

If the medium in which the radiation propagates has $\tau_2 - \tau_1 >> 1$, it is called optically thick. This means $I(s_2) = j/\alpha$. The emitted radiation of this frequency gets absorbed completely before it gets re emitted again. As α is dependent on frequency this condition may not hold for all frequencies. For a tokamak plasma an electron cyclotron frequency satisfies the condition. This means the medium is a black body. All black bodies radiate at an intensity

$$I(\nu) = \frac{\nu^2}{c^2}\frac{h\nu}{\mathrm{e}^{h\nu/k_BT} - 1}, \tag{19}$$

which is also called Planck's law. For low frequencies compared to the thermal energy $h\nu \ll k_BT$ this can be approximated as

$$I(\nu) = \frac{\nu^2 k_B T}{c^2}. \tag{20}$$

As this last condition is easily satisfied in a fusion plasma the intensities measured at electron cyclotron frequencies are directly proportional to the electron

temperatures at the location of emission in the plasma. Now it is known that electrons radiate with a intensity determined by their temperature at the electron cyclotron frequency. The next subsection will explain how a 2D image can be created by using the properties of cyclotron radiation

3.3 Electron temperature profile measurements

The dependency of the electron cyclotron radiation frequency on the magnetic field and its intensity on temperature allows for the detection of electron temperature profiles in a tokamak reactor. This is because the toroidal magnetic field in a tokamak is not constant in the entire plasma volume but has a gradient proportional to $1/R$ where R indicates the major radius. This means every radial position has its own absolute magnetic field strength and thus its own cyclotron frequency. By installing antennas that detect multiple frequencies and using the known toroidal magnetic field one can get a radial profile measurement of the electron temperature. To also measure the temperature in the vertical direction one can stack sets of these antennas detecting different frequencies with each set receiving light from a narrow sight line in the plasma. This kind of antenna array is known as an Electron Cyclotron Emission Imaging (ECEI) system. An ECEI system therefore has the ability to make non invasive 2D cross section images of the electron temperature in a tokamak plasma. As the experiments in this report are done at KSTAR with its ECEI system the next subsections will explicate the reactor and its systems.

3.4 KSTAR reactor

The KSTAR reactor is a tokamak with a major radius of 1.8m and a minor radius of 0.5m. With a triangularity of 0.8 and an elongation of 2 the KSTAR magnetic flux surfaces have a non circular cross section as shown in a simulation of the equilibrium magnetic field in figure (3). The KSTAR tokamak can drive a maximum plasma current of 2 MA and achieve a maximum on axis toroidal magnetic field of 3.5 T. The coils that induce the toroidal magnetic field of KSTAR are superconducting which allows for longer operating times than reactors without superconducting coils and for stronger magnetic fields. The KSTAR reactor also has two ECRH gyrotrons that can deliver the modulated heating necessary for this experiment where one can heat at a electromagnetic wave frequency of 105 GHz and the other at 170 GHz. To detect cyclotron radiation emitted by the tokamak plasma the KSTAR reactor has an ECEI diagnostic which is further explained in the following subsection.

3.5 KSTAR ECEI system

The KSTAR ECEI system consists of 3 systems. Two systems are installed at the H-port and can observe two different radial ranges of the cross section at that location. The third system is located at the G-port toroidally separated from the two other systems by 22°. Figure (4) shows a depiction of the setup from the works of G.S. Yun [11] [12]. The setup consists of a set of lenses to focus the radiation, a beam splitter at the H-port and a heterodyne detection system. The heterodyne detection system makes use of local oscillators to mix the signal with a chosen frequency such that the difference between the local

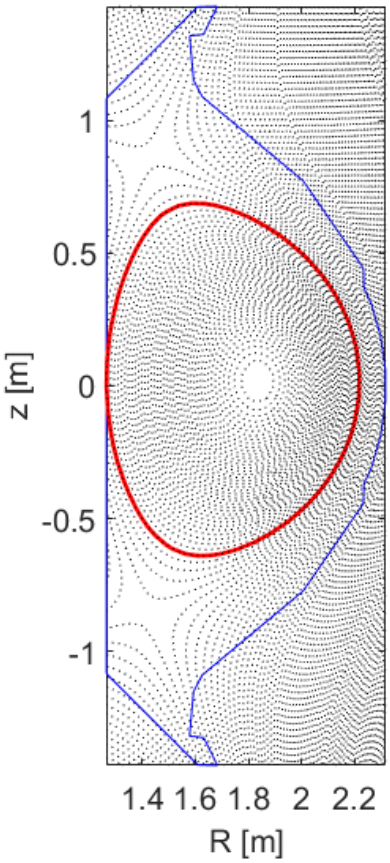

Figure 3: Simulation of the cross section of the KSTAR tokamak showing the equilibrium magnetic field flux surfaces in black. The blue line indicates the edge of the vacuum vessel and the red line indicates the last closed flux surface.

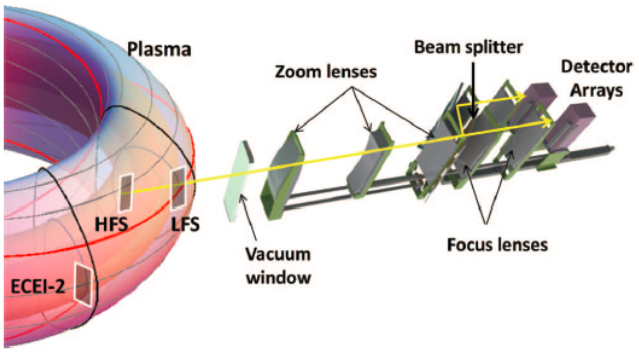

Figure 4: A depiction of the KSTAR ECEI systems named HFS and LFS. The observation surfaces HFS and LFS are located at the same toroidal angle. They simultaneously observe two radial locations by making use of a beam splitter and two local oscillators which can be set to different frequencies in combination with two antenna arrays. The second ECEI system named the G-port system has a similar setup without the beam splitter but with some differences to increase the signal to noise ratio. Details of specific components and the original image can be found in the works of G.S. Yun [11] [12].

oscillator frequency and the signal frequency can be detected by an detector array. This down conversion of the frequency is necessary as there exist no efficient detection systems for frequencies in the range of 100 GHz and above. All three systems have an antenna array of 24 vertically spaced sets of antennas that detect 8 frequencies going from 2.6 GHz to 8.9 GHz. The vertical spacing of the antennas in combination with the zoom of the lenses can image from 30 cm up to 90 cm vertically. The different antennas in combination with the local oscillator can detect frequencies in the range of 75-130 GHz. As the cyclotron frequencies emitted by the plasma are dependent on the magnetic field (see equation 14), the choice of magnetic field influences the measurement location together with the local oscillator frequency. To manually adjust the measurement location the local oscillator frequency can be varied. These parameters lead to a typical observation window in a 2 T magnetic field of 46 cm vertically and 12 cm radially with a vertical resolution of 2 cm and a radial resolution of 1.5 cm. Every one of the three systems also has a time resolution of 2 µs or alternatively a sampling rate of 0.5 MHz.

The detection of the electron cyclotron radiation by the ECEI system can be done for O-mode radiation and X-mode radiation polarization. Where O-mode represents a wave polarized with the electric field parallel to the magnetic field of the plasma and X-mode represents a wave polarized with the electric field partially transverse to the magnetic field of the plasma and partially longitudinal. The best polarization for detection depends on the plasma parameters as the O-mode has a cutoff (propagation frequency limit) at the plasma frequency and the X-mode has a cutoff at the upper hybrid frequency. This is depicted in figure (5). When the magnetic field is high enough ($B \geq 2.5$ T) the fundamental O-mode can be used for measurements. For a low magnetic field (~ 2 T) or a high density plasma the fundamental cyclotron frequency is not accessible in

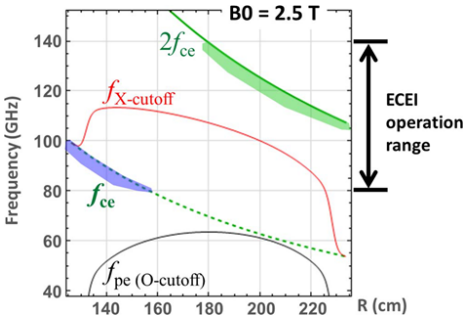

Figure 5: Example of cyclotron frequencies and cutoffs in a 2.5T plasma at KSTAR. The black range indicated on the right of the figure shows the ECEI system frequency range. The colored areas under the first and second harmonic (f_{ce} and $2f_{ce}$) show the radii that fall within this frequency range. The red and black lines shot the cutoffs for the X- and O-modes respectively. The image originates from the work of G.S. Yun [12].

either O-mode or X-mode. In this case the second harmonic in X-mode is therefore used for measurements. Figure 5 shows the values of the first and second harmonic as well as the cutoffs for O- and X-mode in a 2.5 T KSTAR plasma (made by G.S. Yun [12]).

3.6 Summary

This section showed the properties of electron cyclotron radiation and how it can be used to detect electron temperature profiles in 2D. The key property is the proportionality of the electron cyclotron frequency to the magnetic field strength such that each radial position in a tokamak radiates at its own frequency. In combination with the black body radiation linking the intensity of cyclotron radiation to the local electron temperature these frequencies allow the detection of a electron temperature profile. By using an array of antennas one can then create an ECEI system that can take 2D electron temperature images of a tokamak cross section. The KSTAR reactor and its ECEI system are described as well as the different polarizations and harmonics accessible to detect electron cyclotron radiation. The next section will show a short summary of the results from M.J. Choi [2] using the KSTAR system which is the base for the second research question of this report.

4 Turbulence near a magnetic island

As described in the introduction and in section 2, magnetic islands are known to act as a shortcut for heat transport by guiding energy along their outer flux surface, reducing the energy confinement time. Magnetic islands can also become unstable and disrupt the plasma completely when they grow beyond a certain width. But recently it has appeared that the influence of magnetic islands on the plasma is not limited to these effects. It has been observed that the presence of a magnetic island can result in two scenarios for the electron temperature as sketched in figure (6). In figure (6a) the magnetic island acts as a fast transport channel resulting in an unchanged temperature gradient on the inboard side of the magnetic island and a lower core temperature. Figure (6b) shows the more recently found alternative scenario. Here the inboard side of the magnetic island acts as a transport barrier and the temperature gradient increases. Allowing for a possible higher core temperature and better energy confinement.

In KSTAR the scenario where a magnetic island creates a transport barrier has been observed in shot #13371. The radial electron temperature profile for shot #13371 is displayed in figure (7). To find an explanation for the increased electron temperature gradient a paper by M.J. Choi [2] has analyzed the electron temperature turbulence. M.J. Choi finds that near magnetic islands exist areas with varying degrees of temperature turbulence and poloidal flow. A result from his paper is shown in figure (8). The figure shows calculations for the electron temperature turbulence in (8a) and (8b) and for the poloidal flow in (8c) calculated by using vertically adjacent channels. M.J. Choi observed that the area near the X-point has more turbulent fluctuations than near the O-point. Besides this the poloidal flow and radial poloidal flow gradient are higher near the O-point. It is suggested by M.J. Choi that the shear created by the poloidal flow gradient reduces the size of the turbulent structures near the O-point resulting in the observed turbulence differences between O- and X-point. The turbulence reduction by shear could then also cause lower flux surface averaged transport as part of the turbulence on the inboard side of the magnetic island is suppressed. This could then be causing the observed increase in temperature gradient on the inboard side of the magnetic island. The following sections aim at answering the question: Can we directly measure a difference in thermal transport between the inboard side of the magnetic island compared to the unperturbed section of the tokamak plasma?

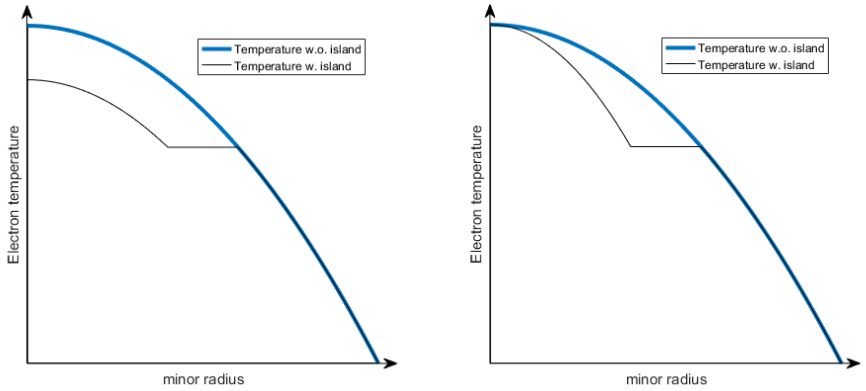

(a) Island acts as a fast transport channel

(b) Island acts as a transport barrier

Figure 6: Sketch of the two scenarios for the electron temperature profile as a function of minor radius with the presence of a magnetic island. If the magnetic island acts as a fast transport channel the gradient of the temperature is unchanged as depicted in figure (a). If the magnetic island creates a transport barrier on the inboard side the temperature gradient will increase which results in figure (b).

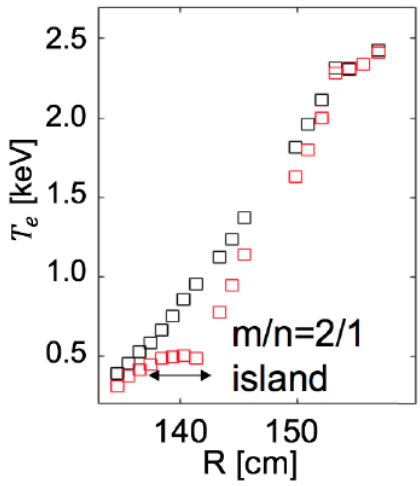

Figure 7: Image from the work of M.J. Choi [2] depicting the 1D temperature profile of a KSTAR shot containing a magnetic island in red and before the island appears in black. The black arrow shows the temperature flattening at the location of the magnetic island. An increased temperature gradient can be seen on the inboard side of the magnetic island.

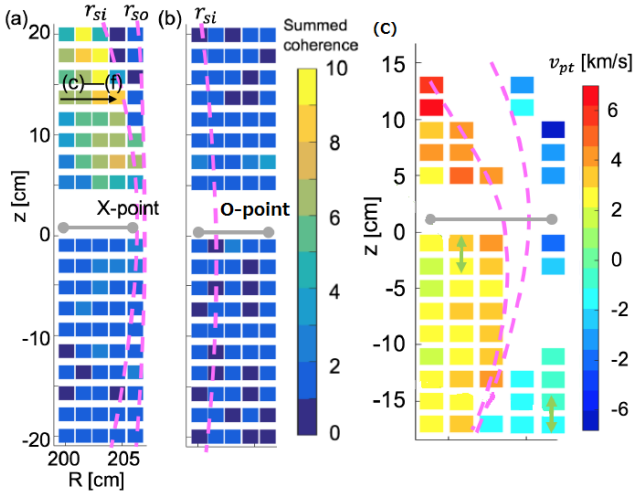

Figure 8: A plot of the results of turbulence and poloidal flow measurements near a magnetic island. The experiment was done by M.J. Choi [2] on KSTAR shot #15638 for (a) and (b) and #13371 for (c). r_{si} and r_{so} indicate the inner and outer separatrix of the magnetic island. It was found that there exists an area with high turbulence near the X-point compared to the O-point of the magnetic island shown in (a) and (b). Sub figure (c) shows high poloidal flow near the O-point and lower poloidal flow near the X-point. The gaps in these graphs are data points omitted due to low accuracy.

5 Signal analysis

This section will explain the general data processing done to arrive at the physical quantities phase and amplitude of the heat wave that are used in the equations of section 2 for the approximation of the heat diffusion coefficient.

5.1 The Fourier transform

One of the most used and well known analysis methods for periodic signals is the Fourier transform. This transform maps any function onto an orthogonal basis consisting of the cosine and sine functions by means of the transformation function

$$F(\omega) = \int_{-\infty}^{\infty} f(t)e^{-i\omega t}\mathrm{d}t. \tag{21}$$

A Fourier transform creates a complex function $F(\omega)$ from the function $f(t)$ that is dependent on frequency instead of time. The purpose of transforming a signal to the frequency domain is generally the analysis of specific frequency components in the signal and filtering of noise. One of the limitations of the Fourier transform however, is that all time information is lost, i.e. the Fourier transform shows the frequency components but not when they are present in the time domain. The Fourier transform is therefore ideal for periodic signals with a constant frequency composition and amplitude.

5.2 Error on Fourier components

To calculate the phase and amplitude of a heat wave of a constant frequency from a time window of ECEI data one can apply the Fourier transform. This will yield complex Fourier coefficients for all the frequencies present in the signal. The absolute value of the complex Fourier component belonging to the heat wave frequency will give the amplitude of the wave and the angle of the complex Fourier component with the real axis will yield the phase. However, applying one single Fourier transform over the time window will give no indication of the error made on the calculation of the amplitude and phase. To calculate the error caused by white noise components another calculation can be used. Assuming the noise is Gaussian distributed and constant in amplitude over time, reasonable assumptions for thermal noise in a stable plasma, there is a method for estimating the error made on the calculation of the Fourier components. By splitting the time domain in smaller pieces and applying the Fourier transform separately on each piece an indication of the fluctuation of the Fourier components can be found. In [9] it is shown that for a stable plasma with no time localized temperature perturbations in the measurement window, the complex Fourier coefficients are distributed Gaussian in both complex an real components with one general standard deviation σ. This means an average of complex Fourier coefficients from smaller time windows gives the complex Fourier coefficient of the larger time window. The error on phase and amplitude can be estimated with the variance of the Fourier coefficients making up the average. To calculate the average and variance for Fourier coefficients the following equations can therefore be used [9]:

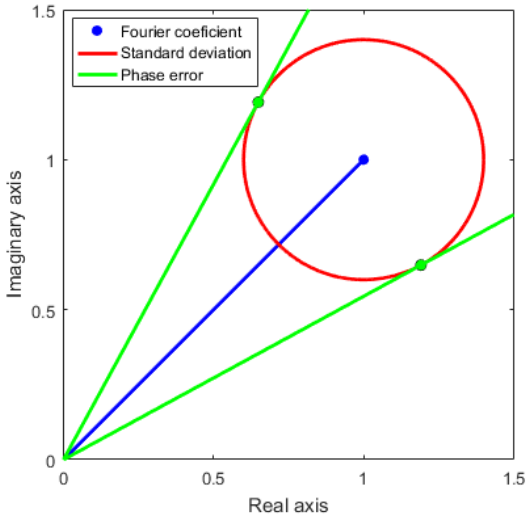

Figure 9: This figure shows a representation of the mean and variance calculated by means of equation 22 and 23. The blue dot represents the time averaged Fourier coefficient ($\langle\Theta\rangle$), while the red circle indicates the standard deviation calculated from the variance (σ^2). The green lines indicate the minimum and maximum phase angle where all points within the standard deviation lie.

$$\langle\Theta\rangle = \frac{1}{M}\sum_{m=1}^{M}\Theta^{[m]} \tag{22}$$

$$\sigma^2 = \frac{1}{M(M-1)}\sum_{m=1}^{M}\left|\Theta^{[m]} - \langle\Theta\rangle\right|^2 \tag{23}$$

Where $\langle\Theta\rangle$ represents the average complex valued Fourier coefficient over the time window and σ^2 the variance of that average. Note that the variance is always a real value indicating the absolute deviation from the average of the complex values in both real and imaginary direction. Figure (9) displays a representation of the complex average and the standard deviation calculated from the variance in the complex plane. For the calculation of the approximation of the heat diffusion coefficient from subsection 2.1 however, one needs the amplitude and phase of the complex Fourier component for a heat wave frequency.

The error on the amplitude and phase of a Fourier coefficient are noted to be a Rician and Rician phase distribution respectively in the work [9]. These Rician distributions have the property that they tend towards a Gaussian distribution in the limit of amplitude over standard deviation: $A/\sigma \to \infty$. In [9] it is stated that for $A/\sigma > 5$ the use of a Gaussian approximates the statistical error boundaries of the Rician distributions well. As can be observed from figure (9), for a Gaussian distribution the error on the amplitude is simply the standard deviation on the Fourier coefficient. But, the derivation of the error on the phase from the standard deviation is not as straightforward. It can however be seen from figure (9) that the error on the phase angle depends both on the mean

value of the complex Fourier component and the standard deviation. As a lower amplitude with the same standard deviation will mean the red circle moves closer to the origin and thus the angle being covered by the circle is bigger. The brute force way to determine the standard deviation of the phase is to create a distribution based on the mean Fourier coefficient and the standard deviation and calculate the phase for all values in the distribution. Here, however, will be suggested an alternative method based on the geometry of figure (9). The points of maximum and minimum phase on the red circle representing the standard deviation of the Fourier coefficient should also be an indication of the standard deviation of the phase for this coefficient. These points should easily be found if the system is transferred to a polar coordinate system as such:

$$r^2 + A^2 - 2rA\cos\theta = \sigma^2 \tag{24}$$

Where $A = |\langle\Theta\rangle(\omega)|$ and σ^2 is the variance. By finding the minimum and maximum θ for this circle an approximation can be found for the standard deviation of the phase as a function of amplitude and variance. This can be done by calculating the derivative:

$$\frac{\partial\theta}{\partial r} = \frac{\partial}{\partial r}(\arccos\frac{r^2 + A^2 - \sigma^2}{2rA}) = 0 \tag{25}$$

Which results in

$$\frac{\partial\theta}{\partial r} = \frac{A^2 - \sigma^2 - r^2}{Ar^2\sqrt{-\frac{A^4 - 2A^2(\sigma^2 + x^2) + (\sigma^2 - r^2)^2}{A^2 r^2}}} = 0 \tag{26}$$

Which has the solution for r

$$r = \sqrt{A^2 - \sigma^2} \tag{27}$$

Substituting r in equation 24 and solving for θ, results for the standard deviation on the phase:

$$\theta_{max} = \arccos\left(\frac{\sqrt{A^2 - \sigma^2}}{A}\right) = \sigma_\phi. \tag{28}$$

Note that this equation does not give a real valued solution for $\sigma^2 > A^2$ which can be understood as under this condition the standard deviation of the Fourier coefficient crosses the origin. If the standard deviation crosses the origin any phase is possible and the idea of phase boundaries is no longer valid. The solution derived here for σ_ϕ can be compared with the brute force solution of creating a sampled Gaussian distribution with random numbers as mentioned before. The results can be seen in figure (10). Here the relative error of the approximation σ_ϕ to the actual 68% boundaries for the phase angle calculated from a Gaussian distribution of Fourier coefficients is plotted as a function of the ratio A/σ. For the region of non-Gaussian phase distribution the 68% boundaries are defined as the 68% sample points closest to the highest probable value. In figure (10) can be seen that the approximation σ_ϕ quickly approaches the actual standard deviation and seems lo level out at 0.1% relative error. The fluctuation on the values of figure (10) is caused by the random numbers used to create the phase distribution. Note that the phase distribution can be accurately approximated from $A/\sigma > 5$ and thus the approximation is accurate for the entire domain in which the phase distribution can be approximated by a Gaussian distribution.

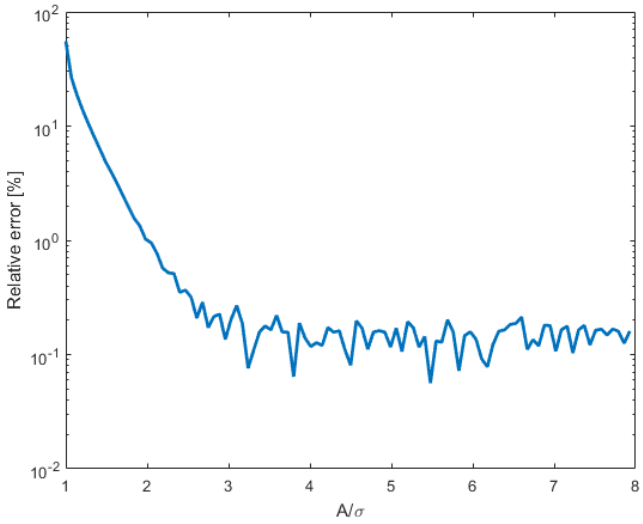

Figure 10: Depicted in this figure is the relative error of the approximation from equation 28 to the actual 68% error boundaries of a distribution of the phase of a Fourier coefficient with a standard deviation σ and amplitude A. For a ratio of $A/\sigma > 5$ the distribution of the phase can be approximated by a Gaussian as stated in [9]. It can be seen that the relative error tends towards 0.1%.

5.3 Summary

This section explained the data processing used for analysis of the ECEI data. The calculation of amplitude and phase from the Fourier coefficients was explained and how the error of these two quantities behaves. The next section will apply the Fourier transform to experiments. The method will be shown to be consistent in 1D with a result acquired in a different work. After which, the method will be expanded to 2D.

6 Calculating thermal transport coefficients from ECEI data in 1D and 2D

This section will present the results of the application of the proposed method for calculating the heat diffusion coefficient developed in this work. It will also address the first research question of this thesis. Can a 1D diffusive heat transport model describe a 2D measurement of the thermal transport in a tokamak? The method will first be demonstrated with a 1D line of sight on the horizontal axis of the tokamak and compared with a previous experiment. After this comparison, the measurement will be expanded to 2D and the cylindrical plasma assumption and heat diffusion coefficient approximation will be tested.

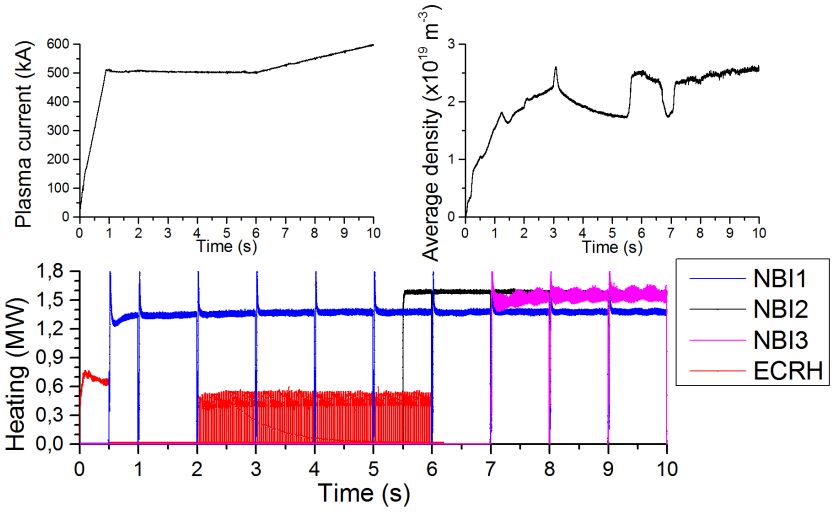

Figure 11: The conditions of shot #12864. After plasma startup indicated by the sharp initial rise in plasma current the modulated ECRH with a frequency of 25 Hz is turned on from 2 seconds up to 6 seconds as can be seen in the heating plot. This shot has a constant toroidal magnetic field with an on axis value of 2.9 T and does not use any kind of magnetic perturbations.

6.1 Thermal transport in 1D

For the calculation of the thermal diffusion coefficient in 1D KSTAR shot #12864 will be used. This shot consists of a stable plasma with modulated ECRH heating of 25 HZ. Figure (11) shows the plasma current, average density and heating power for KSTAR shot #12864. After plasma startup shown by the steep slope of the plasma current, the plasma current is kept stable. The modulated ECRH is injected from 2 to 6 seconds at major radius R = 1.72 m. This is the time window for the heat diffusion measurement. A single sight line of the ECEI system can be used to calculate the diffusion coefficient in 1D. A horizontal sight line is chosen at $z \approx 0$ because this sight line is perpendicular to the flux surfaces and thus measures the radial temperature profile. An indication of the sight line is depicted by the black solid line in figure (12). The

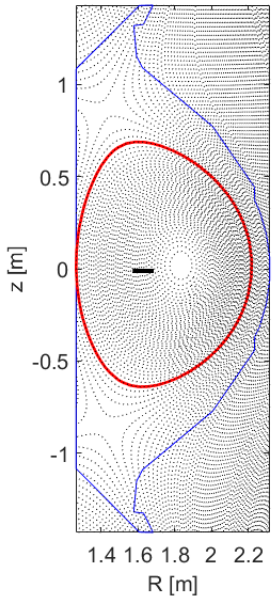

Figure 12: A plot of figure 3 of the KSTAR reactor magnetic flux surfaces with a Thick black line indicating the line of sight for the 1D measurement of the heat diffusion coefficients in shot #12864.

radius is normalized by dividing through the minor radius.

Figure (13) displays the amplitude and phase of the temperature perturbation caused by the MECRH as a function of normalized minor radius calculated with use of the Fourier transform over the time window from 3.5 to 4.5 seconds. This time window was chosen as it is the longest constant temperature window within the activation time of the MECRH and avoids the density fluctuation at 3 seconds that can be seen in figure (11). As calibration data for the temperature was not available for this shot the amplitude of the temperature fluctuation induced by the MECRH is depicted as a relative value. Due to the linear relationship between the ECE radiation intensity and the temperature as shown in equation 20, the relative temperature perturbation can be calculated from uncalibrated data after background radiation subtraction as:

$$\frac{s- < s >}{< s >} = \frac{T- < T >}{< T >}. \tag{29}$$

Where s represents the uncalibrated data, T the temperature and the brackets represent an average over time. This equation will be slightly shortened for convenience to $\frac{dT}{< T >}$. The phase of the heat wave is normalized to the phase of the injected modulation at the main frequency of 25Hz.

The local heat diffusion coefficient can now be calculated by means of the approximations from equation 11 or 12. For this experiment initially equation 12 will be used, the choice of which will be discussed on acquiring values for χ. To use equation 12, a gradient has to be calculated from the phase and ampli-

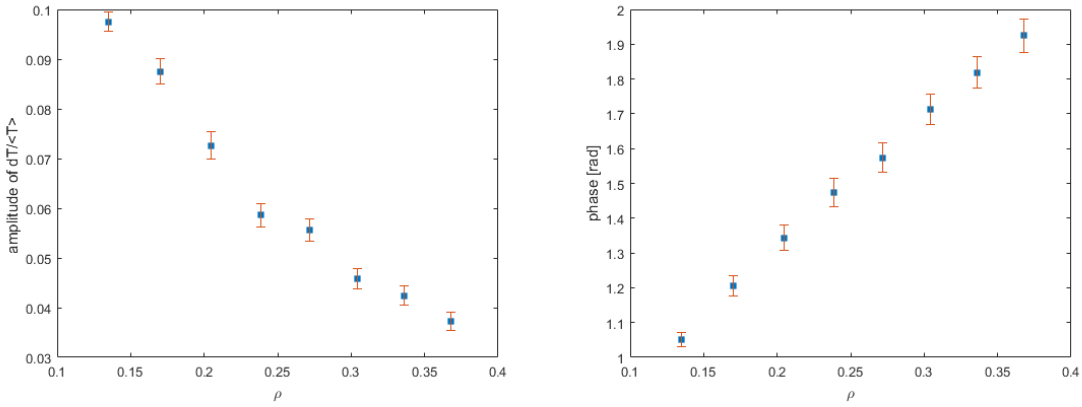

(a) amplitude (b) phase

Figure 13: Amplitude and Phase calculated with the continuous wavelet transform over a single sight line as a function of normalized minor radius from KSTAR shot 12864. Both figures seem to adhere to the behavior expected from the theory.

tude. This work uses a linear gradient calculation between adjacent channels in such a way that the gradient of amplitude and phase can be determined locally. The thermal transport coefficients calculated through this method are shown in figure (15). The error on the diffusion coefficients is found by using error propagation throughout the calculation of the diffusion coefficient. This means that an approximation of the Gaussian distribution of the amplitude and phase values is created based on the standard deviation of the phase and amplitude multiplied with a collection of random numbers. The whole distribution for amplitude and phase is put through the calculation of the heat diffusion coefficient. This will then result in a distribution of heat diffusion coefficients. From this distribution the highest probability value can be taken to be the expectation value and the error deviation can be defined as the 34% points above and 34% points below the highest probability. These definitions are necessary due to the non-Gaussian distribution of χ. Of which an example can be seen in figure (14). This figure shows the distribution function of the heat diffusion coefficient at $\rho = 0.37$. It is observed that a higher relative error on the phase gradient and amplitude results in a significantly higher upper error on the heat diffusion coefficient. In the figure it can be seen that the probability distribution has a long tail towards higher χ. This means the accuracy of the amplitude and phase data is hugely influential on the accuracy of χ.

Calculating the expectation value and error boundaries for the 68% interval results in figure (15). The results from figure (15) can be compared with results from a paper by T.Kobyashi done on the same KSTAR shot #12864 [13]. T.Kobayshi assumes constant values for φ' and A'/A and this results in $\chi \approx 1m^2/s$ as an average for the measurement volume. The value of $\chi = 1m^2/s$ is indicated in figure (15). It can be observed that the local electron heat diffusivity values calculated in this work lie near the average value calculated by T.Kobayashi.

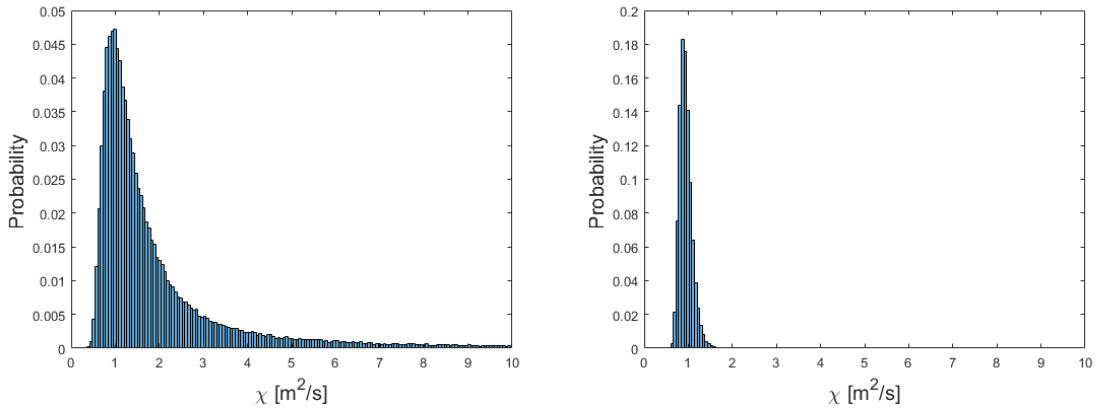

(a) $\rho = 0.37$ (b) $\rho = 0.17$

Figure 14: Heat diffusion coefficient probability distributions at $\rho = 0.37$ and $\rho = 0.17$. Both distributions are a non-Gaussian, but the probability function for $\rho = 0.37$ has a long tail towards higher χ. Meaning that the upper uncertainty boundary is significantly higher than at $\rho = 0.17$. The upper error boundary shows a strong dependency on the relative error in amplitude as the absolute error at both locations is comparable (see figure (13)).

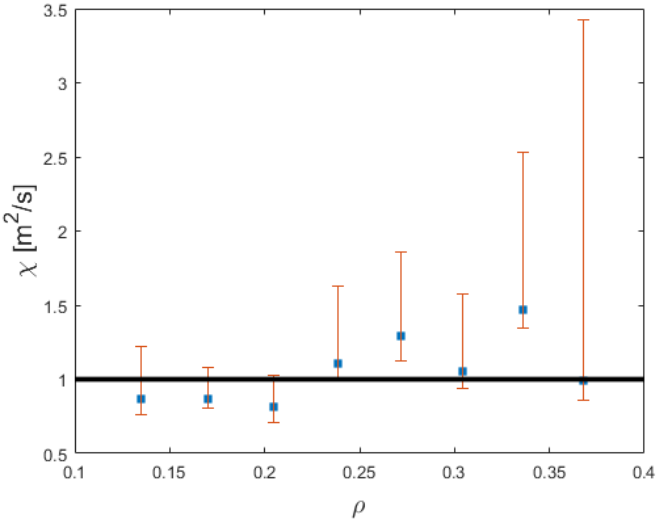

Figure 15: Heat diffusion coefficient χ as function of normalized minor radius calculated over a single sight line. The black line indicates the value of χ ($\chi = 1.0m/s^2$) as calculated by T. Kobayashi [13].

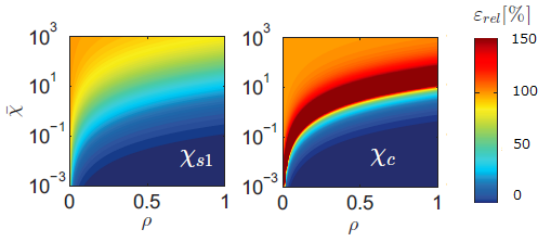

Figure 16: Figure from the work of M.Berkel [9] indicating the relative error ($\epsilon_{rel} = (\chi_{approx} - \chi)/\chi$) of approximations of the heat diffusion coefficient for the parameter space of normalized radius ρ and normalized diffusion coefficient $\bar{\chi} = \chi/\omega$. Where $\chi_{s1} = \chi_1$, $\chi_c = \chi_2$ and ω is the ECRH modulation frequency multiplied with 2π.

The values for χ from figure (15) can now also be used to review the choice of approximation from the two equations found in section 2 (equation 11 and 12). In the work of M.berkel [9] a multitude of approximations for the heat diffusion are examined by their relative error to the true value of the heat diffusion coefficient ($\epsilon_{rel} = (\chi_{approx} - \chi)/\chi$). Figure 16 shows the results for the equations from section 2 in the parameter space of ρ and $\bar{\chi} = \chi/\omega$. Where $\chi_{s1} = \chi_1$, $\chi_c = \chi_2$ and ω is the modulation frequency times $2\,\pi$. From this figure it can be seen that for the parameter space of this experiment ($0.1 < \rho < 0.4$ and $\bar{\chi} \approx 6 \cdot 10^{-3}$) equation 11 will give a higher relative error than the other approximations. It is also clear that from these 2 approximations, equation 12 would have the biggest parameter space with a low error. However, it has to be considered that this figure displays the error made by the approximation compared to the true value and does not include error boundaries on the input values.

6.2 2D thermal transport in steady state plasmas

The 1D calculation of the heat diffusion coefficient has shown agreement with a previous measurement and has shown that the best approximation equation in the parameter space of this experiment is equation 12. As subsection 6.1 used only a subset of the data from the ECEI system the other channels can be used to expand to 2D and examine the assumptions made in the derivations of subsection 2. In particular the cylindrical approximation and the transport model equations. To do this both the higher harmonics of the modulation frequency and different propagation angles will be examined. As in the previous section this will be done on KSTAR shot #12864. The measurement surface for the 2D measurement is indicated by a black box in figure (17). Figure (18) shows the relative amplitude and phase of the 25Hz main component of the temperature modulation plotted on the equilibrium magnetic flux surfaces. The phase is normalized to the 25Hz component of the MECRH source. In figure (18) the source of the heat wave coming from major radius $R = 1.72m$ is clearly visible by the profiles showing symmetric profiles around the axis $z = 0$ and a higher amplitude and lower phase on the right side of the figures. This gives an indication of the expected radial propagation of the heat wave. If

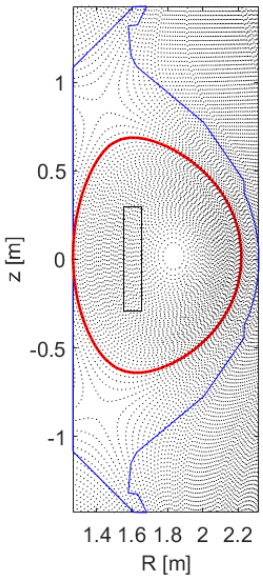

Figure 17: A plot of figure 3 of the KSTAR reactor equilibrium magnetic flux surfaces with a black box indicating the measurement surface for the 2D measurement of heat diffusion coefficients in shot #12864.

the approximation of the cylindric plasma holds true the measured phase and amplitude from figure (18) should be flux functions. To test this figure (18) is interpolated on multiple lines perpendicular to the flux surfaces.

Figure (19) displays linearly interpolated points created under the angles θ: $-58°$, $-40°$, $-20°$, $0°$, $20°$, $40°$ and $58°$ with the negative horizontal axis. The cross section of the interpolated lines is at the center of the last closed flux surface as this flux surface is the least affected by the Shafranov shift. With positive angles defined in the counter-clockwise direction. If the amplitude and phase values along these lines as a function of the normalized radius ρ are the same for all angles the assumption of 1D thermal transport holds. As the KSTAR magnetic flux surfaces are not circular but more elliptical the equation for ρ can be redefined to transform coordinates from an elliptical space to a circular space:

$$\rho = \frac{\sqrt{(R - R_0)^2 + (\frac{a_R}{a_z}(z - z_0))^2}}{a_R} \tag{30}$$

Where R_0 is the radial middle of the plasma, z_0 is the vertical middle of the plasma, a_R is the minor radius in the radial direction and a_z is the minor radius in the vertical direction determined from the equilibrium magnetic flux surfaces. Equation (30) does not take into account the triangularity of the KSTAR plasma as this is expected to have a negligible effect on measurements on the high field side of the plasma. Plotting the different angles from figure (19) as a function of ρ then results in figure (20). The error on the phase and amplitude in figure (20) are taken as the error on the nearest neighbor to the interpolated grid point. These two figures show that under any of the angles θ the amplitude and phase

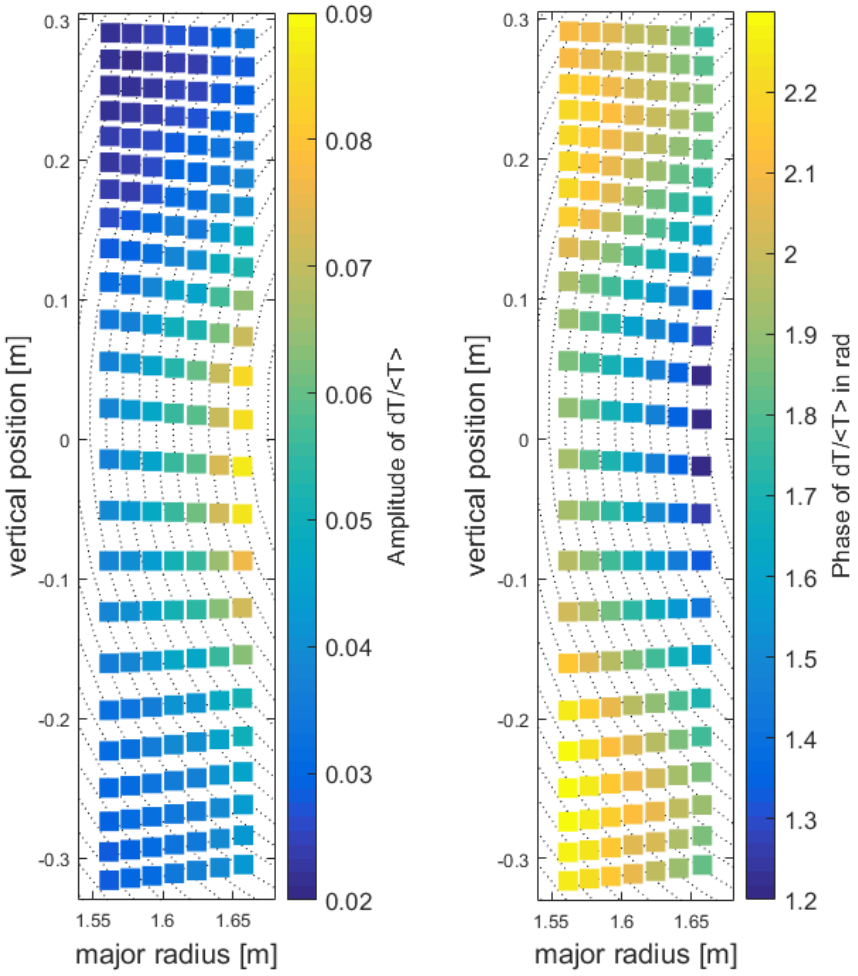

(a) Amplitude

(b) Phase

Figure 18: Measured amplitude and phase of the 25Hz main component of the heat pulse injected by the MECRH system for KSTAR shot #12864. Below the pixels indicating the amplitude and phase the equilibrium magnetic flux surfaces are plotted as dotted lines.

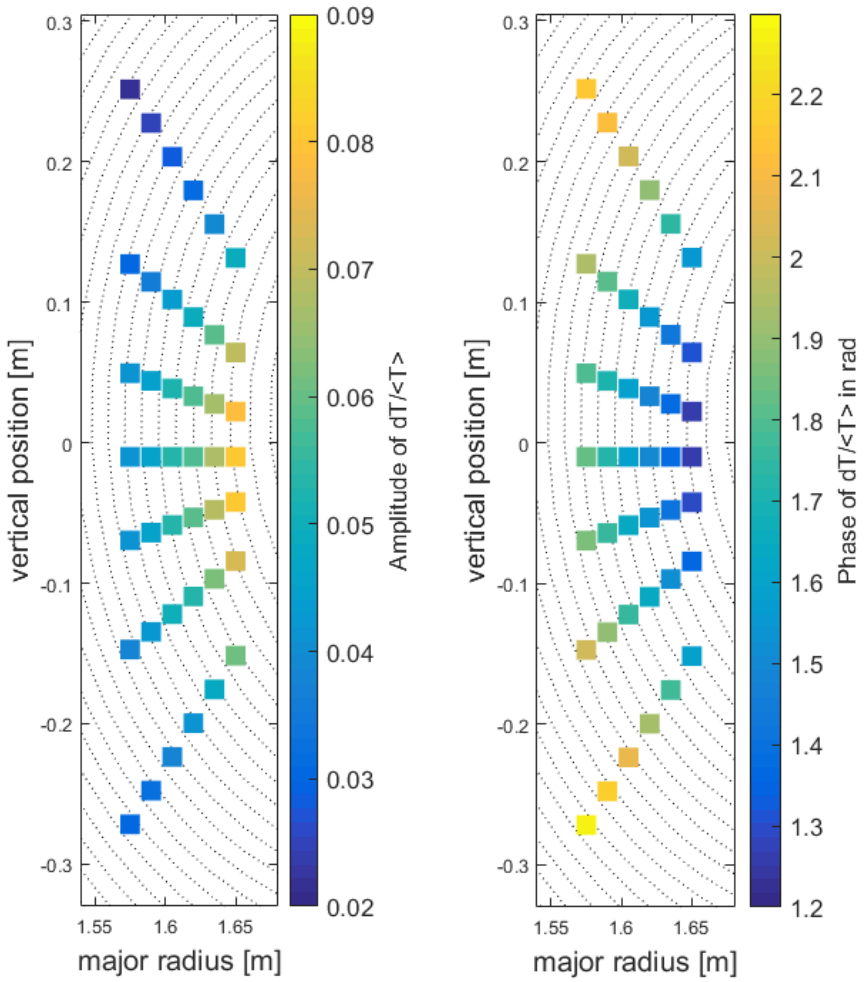

(a) Amplitude

(b) Phase

Figure 19: Interplolation points for amplitude and phase under multiple angles plotted on the equilibrium magnetic flux surfaces.

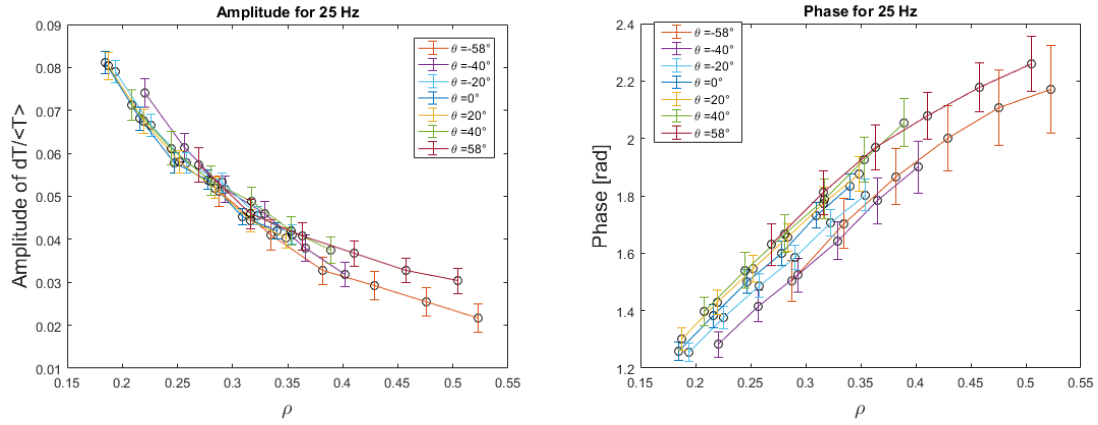

(a) amplitude (b) phase

Figure 20: Amplitude and phase of the 25Hz component of the MECRH induced heat wave as a function of ρ defined by equation 30. The values of the amplitude and phase show similar and overlapping values for the measurements under every angle. Therefore confirming transport of the heat wave perpendicular to flux surfaces.

overlap within the error bars and deliver the same values as a function of ρ. This means the data supports the assumption that the heat wave propagates perpendicular to the flux surfaces.

From the data of figure (20) it is now possible to calculate the thermal diffusion coefficients for the 2D case. Figure (21) displays χ as a function of ρ for all the interpolation angles. Here it can be seen again that due to the higher relative error on data measured at a higher ρ the upper error boundaries can reach tenfold the highest probable value. In the domain of $0.17 < \rho < 0.35$ it seems however that it can be said that the diffusion coefficient is around $1m^2/s$. This agreement between the plots for all interpolation angles is to be expected from the similar values seen for the amplitude and phase in figure (20).

As well as examining the phase and amplitude for different angles it is possible to examine them at different harmonics of the 25Hz modulation. This allows the comparison of the data with equation 7 for the temperature Fourier coefficient. The amplitude and phase of two harmonics with sufficient signal to noise ratio to satisfy the condition for Gaussian distributed phase an amplitude errors is calculated together with the 25Hz component under the angle $\theta = 0°$. A mean of ϕ' and A'/A is calculated such that under slab geometry an average χ calculated by equation 12 can be substituted in equation 7. Then the complex valued equation 7 for the temperature Fourier coefficient is fitted through the data by means of the least squares method to obtain a value for the constant $C_1(i\omega)$. The constant C_2 is zero as reasoned in chapter 2. Both the data and fit are plotted for amplitude and phase in figure (22) . It can be observed from figure (22) that the model does not fit through all of the data points within the 68% error boundaries both for phase and amplitude. A reduced chi-squared analysis $\boldsymbol{\chi}^2_{fit}$(here denoted with the subscript fit and in bold to avoid confusion with the diffusion coefficient) is done on the complex Fourier coefficients

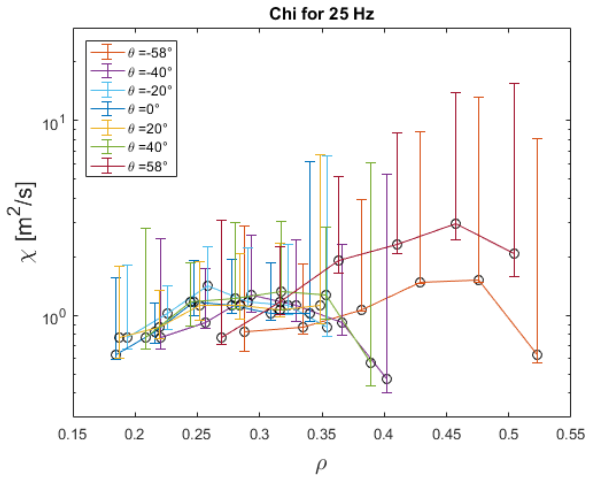

Figure 21: A figure of the heat diffusion coefficient χ as calculated from the 25Hz component of the MECRH induced heat wave as a function of ρ. Where ρ is defined by equation 30. The figure is plotted to a logarithmic scale to include the large error boundaries on χ for larger rho.

to show the quality of the fit. For the 25 Hz data points the model fit gives a $\boldsymbol{\chi}^2_{fit} = 14.4$. This $\boldsymbol{\chi}^2_{fit}$ is significantly higher than one meaning the model does not describe the data well. However this error could be due to the method of estimating χ. A more significant problem with the model equation 7 can be seen by looking at the the harmonics in figure (22). The slope of the model can be seen to be significantly steeper than the data. This hints at an error in the frequency dependence of the model. An explanation for this mismatch is that the local heating profile assumed in the equations is not a delta function at the ECRH deposition location but spread out more along the plasma. This larger heating profile would account for the slower amplitude decay and for the slower phase increase.

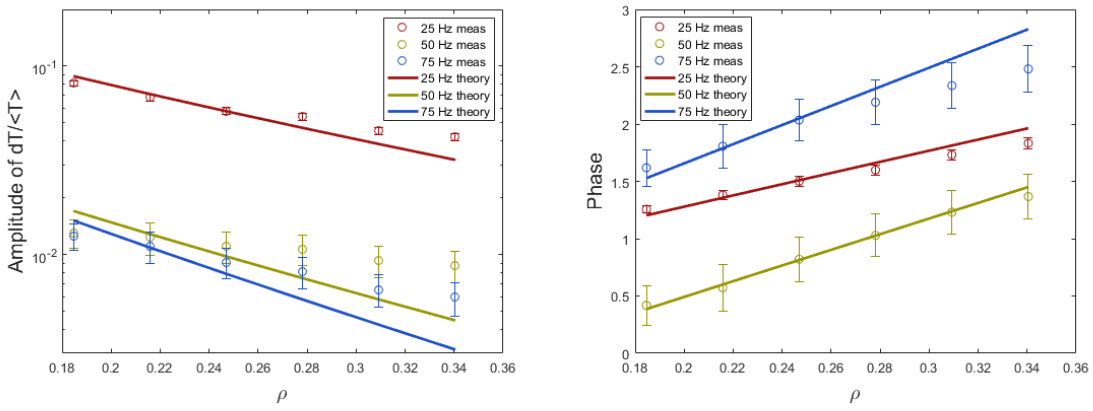

(a) amplitude

(b) phase

Figure 22: Amplitude and phase for multiple harmonics of the heat wave frequency as a function of ρ. As solid lines are plotted the theoretical amplitude decay and phase increase for the average χ as by equation 7. The theory predicts different slopes for both the amplitude and the phase compared to the data.

6.3 Summary

This section has displayed a method of calculating local heat diffusion coefficients from KSTAR ECE data. A comparison is made in a 1D scenario with a steady state plasma and MECRH between the method developed in this work and a calculation done in the work of T. Kobayashi [13]. It is observed that both methods yield similar heat diffusion coefficients within the error. It is also noted that equation 12 has the smallest error in the estimation of the heat diffusion coefficient in the parameter space of the experiment. From the 1D case the calculations are expanded into 2D where the assumptions of 1D heat transport and the transport model are tested. It is found that the 1D transport assumption holds when a correction is made for the ellipticity of the KSTAR plasma. The transport model that leads to equation 7 is however found to not fit the data completely. Indicated by a reduced chi squared of 14.4. It is suggested that the error is caused by an error in the heating profile. Meaning, the heating profile is possibly not as localized as expected from the ECRH theory and is also present in the measurement volume causing slower amplitude decay. The effect of this is especially noticeable at higher harmonics of the heat wave. Therefore, for the use of equation 12, only the main frequency component should be used to estimate the diffusion coefficient.

7 Modulation experiment in the presence of a magnetic island

This section will discuss the experiment done to address the second research question of this thesis. Can lowered electron thermal transport be observed on the inboard side of a magnetic island lower compared to the unperturbed section of the tokamak plasma?. KSTAR shot #18686 has been designed to use an active RMP field to create a $n/m = 2/1$ stationary magnetic island. MECRH is then set to inject close to the plasma core such that the resulting heat wave can propagate past the magnetic island. The three KSTAR ECEI systems are intended to observe the inboard side, the location of the magnetic island and the outboard side of the magnetic island on the low field side of the plasma. This way, the transport in and near the magnetic can be observed.

Figure (23) displays the exact parameters used during KSTAR shot #18686. In this shot, with an on axis toroidal magnetic field strength of 2 T, a 0.7 MW 50Hz MECRH pulse of frequency 105 GHz is injected at R = 1.91 m at the second harmonic resonance of the plasma. Additionally, 1.2 MW neutral beam heating is injected to create a stable temperature profile. The $m/n = 2/1$ magnetic island created by the RMP field appears at R = 2.00 m. The ECEI system named HFS is set to observe $1.82 < R < 1.97m$, the system LFS to observe $2.0 < R < 2.15m$ and the G-port system is set to observe $2.05 < R < 2.2m$. The data from the ECEI systems shows that the HFS system is overexposed and that the LFS system has insufficient signal to noise ratio ($A/\sigma < 1$) for a large number of channels. This leaves only the data from the G-port ECEI system available for analysis. Figure (24) displays the measurement area of the G-port ECEI system inside the KSTAR flux surface simulation. Note that the G-port system measures the outboard side of the position of the magnetic island, such that the main area of interest to answer the research question , namely the inboard side of the magnetic island, is unavailable. Nonetheless, the transport behavior in the G-port area will be examined. Figure (25) shows the amplitude and phase images of a section of data averaged over the window from 5.425 s to 5.625 s. This time window is is chosen due to the 5Hz sawtooth oscillation of the plasma. Because sawtooth crashes cause sudden enhanced transport of energy and particles, the window within two crashes is used for measurements of the heat wave amplitude and phase.

In figure (25) an area of low amplitude and high phase can be observed on the left part of the sub figures. Because transport of heat waves into a magnetic island is typically slow [5] this could indicate the presence of a magnetic island on the left side of the images. As the surface resonant with the RMP field is located around R = 2m for this shot the center of this magnetic island, however, is likely located outside the observation window. The 2D images of figure (25) can be interpolated to map onto lines as a function of ρ just like in section 6. In this experiment as opposed to the previous section, the measurement has a smaller vertical range and is further removed from the flux surface center. Therefore the interpolation angles θ are limited to: $-27°$, $-20°$, $-10°$, $0°$, $10°$, $20°$ and $27°$. Where θ is defined from the horizontal axis with positive angles in the counter clockwise direction. These radial interpolation lines of phase and amplitude are plotted as a function of ρ in figure (26). Where ρ is again defined as in equation 30. Figure (26) shows a similar pattern to the that of figure (20) but reversed

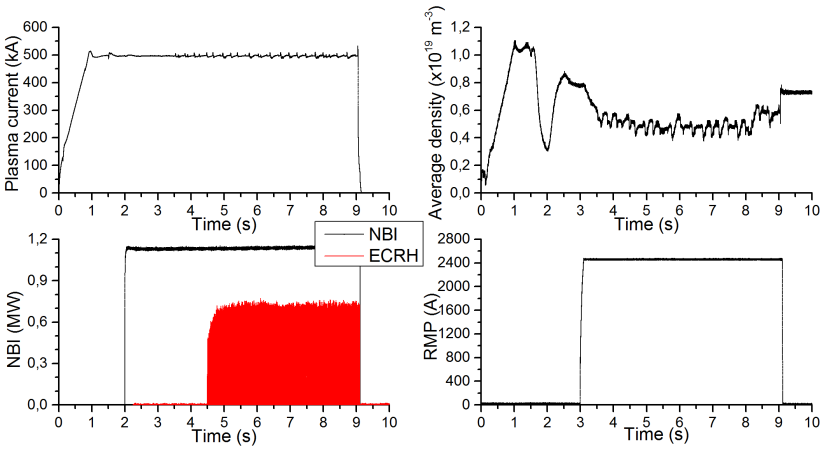

Figure 23: The conditions of shot #18686. After creating a magnetic island with an RMP field at 3 s the MECRH is turned on at 4.5 s. At 9 s the RMP field is turned off and the plasma is stopped at 10 s.

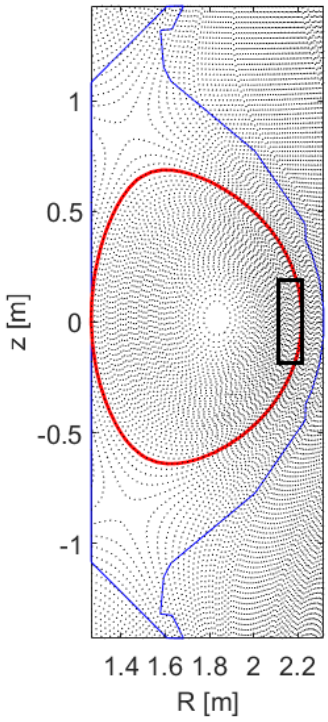

Figure 24: Indication of the measurement surface in the overall magnetic structure of the KSTAR tokamak. The red line indicates the last closed flux surface of the KSTAR tokamak and the purple line indicates the deposition location and propagation direction of the MECRH heat wave. The magnetic island appears at R = 2 m.

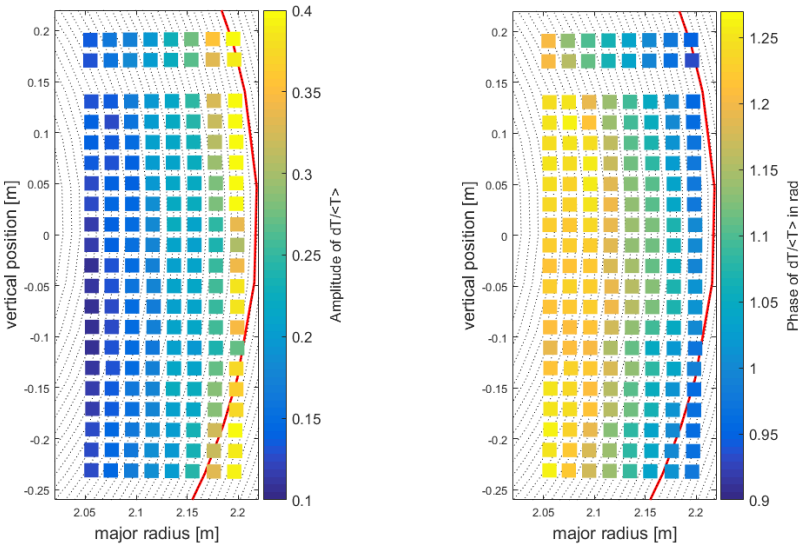

(a) Amplitude (b) Phase

Figure 25: Plots of the amplitude and phase of the MECRH heat wave in KSTAR shot #18686. The left side of both images show signs of the presence of the magnetic island as this area has a low amplitude and high phase typical for the long time necessary for a heat wave to penetrate a magnetic island.

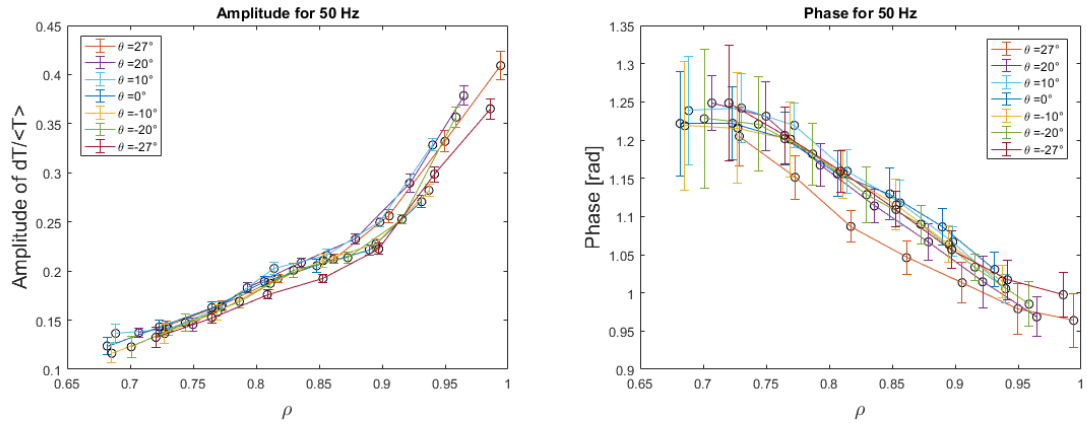

(a) amplitude (b) phase

Figure 26: Amplitude and phase for the 50 Hz component of the heat wave calculated under multiple angles in shot #18686. The heat wave seems to be reversed in direction compared to figure (20).

in dependency on ρ. Measurements of all angles also overlap for amplitude and phase indicating that both are flux functions in the measurement area and that 2D structures like magnetic islands seem to be absent in the measurement area. Although injected at $R = 1.91m$ the heat wave in this measurement area seems to propagate inwards due to an increase in amplitude and decrease in phase for increasing ρ. Other than the location $R = 1.91$ there are however no positions resonant with the injected ECRH at any harmonic. It is suggested here that this could visible be due to the relatively high ECRH power, being 37% of the total heating power. The suspicion of non-localized ECRH heating raised in the previous section could mean figure (25) displays a heat wave originating from energy absorbed at the edge of the plasma traveling inwards.

When looking at higher harmonics of the 50 Hz modulation frequency some other behavior appears. Figure (27) shows the 100 Hz component of the heat wave. Most notable is the maximum in phase located around $\rho = 0.75$. This maximum is removed far from the position $\rho = 0.55$ at which the q=2 surface is located. It can therefore not be the magnetic island. A possible explanation from the assumption of non localized heating could be that at this location the heat wave traveling from the edge of the plasma and the heat wave traveling from the resonance at $\rho = 0.35$ meet creating a local maximum in phase.

7.1 Summary

This section shows a shot from KSTAR aimed at answering the second research question. The ECEI systems of KSTAR were set to observe 3 different sections near the position of a magnetic island induced by a RMP field: The inboard side, the position of the magnetic island and the outboard side. It was found that the high fraction of ECERH heating over the total heating caused the inboard ECEI system to be overexposed. The system aimed hat the position of the magnetic island was troubled by a high number of detectors with low

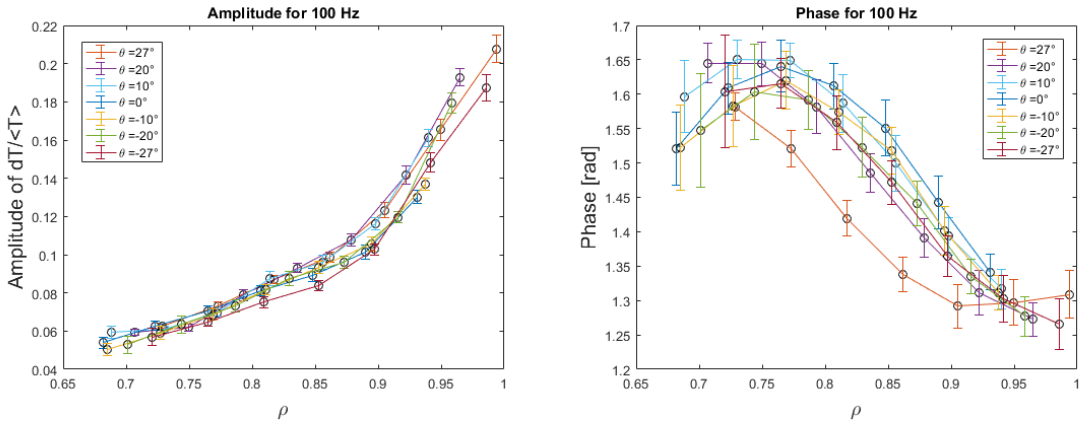

(a) amplitude (b) phase

Figure 27: Amplitude and phase for the 100 Hz component of the heat wave calculated under multiple angles in shot #18686. The amplitude decays but the phase has a maximum near $\rho = 0.75$.

signal to noise ratio ($A/\sigma < 1$) leaving only the outboard system. This means the inboard side relevant to answering the research question is not available and the question can therefore not be answered. The outboard system showed an amplitude and phase profile suggesting a inwards traveling heat wave as opposed to the outwards traveling heat wave expected to originate from the ECRH resonance position. It is then suggested that this could be due to a non localized heating profile where ECRH power is deposited in the edge of the plasma. It is also found that a phase maximum seems to appear at $\rho = 0.75$. An area removed from the position of the q=2 surface at $\rho = 0.55$ where a magnetic island can appear. It is then suggested that this could be a result of a outward heat wave from the plasma resonance position meeting an inwards traveling heat wave from the edge of the plasma.

8 Conclusion and discussion

A method calculating the electron thermal heat diffusion coefficient has been introduced in this work with the goal of testing if a 1D purely diffusive heat transport model can be used to describe the thermal transport of a 2D measurement of a tokamak plasma. This is done with the intention to test if transport barrier behavior can be measured on the inboard side of a magnetic island. The method uses an approximation of an equation for the electron thermal diffusion coefficient under the assumptions of cylindrical geometry and not heating sources present in the measurement volume. It makes use of the propagation of locally injected temperature perturbations. In section 6 measurements have been done on a stable plasma of the KSTAR reactor using an electron cyclotron emission imaging system to analyze perturbations created and locally injected with a modulated electron cyclotron heating system. In Subsection 6.1 a one dimensional measurement has been done to compare calculations of the heat diffusion coefficient with a previous calculation of the heat diffusion coefficient by T. Kobayashi [13] on the same shot. It is found that both calculations show values that are in agreement. Using a figure from the work of M. Berkel [9] it is also concluded that equation 12 is the most accurate of the approximation equations derived in section 2.

Following this an expansion of the measurement is then done into 2D. The 2D measurements of the temperature perturbations are then interpolated to positions on lines intersecting at the center of the last closed magnetic flux surface such that the lines are normal to the flux surfaces. By defining a normalized radius ρ with a correction for the ellipticity of the KSTAR magnetic flux surfaces all the interpolated measurements can plotted as a function of ρ. It is found that the amplitude and phase of the propagating heat wave give similar values for the amplitude and phase under any angle, thus confirming the perpendicular transport and the cylindric plasma assumption used in the derivation of section 2. The assumption of the absence of heating sources in the measurement volume is then tested by fitting the equation 7 predicting the amplitude and phase of a heat wave under the assumptions of the theory onto the data of multiple harmonic components of the heat wave. It is found that the theoretical equation does not predict fit the data well. It is proposed that the difference between the data and theory can be explained if the measurement volume does contain additional heating sources unlike the assumption made in the theory. The answer to the research question: Can a 1D diffusive heat transport model describe a 2D measurement of the thermal transport in a tokamak?. Is then, no. The 1D model does not include terms describing heating in the measurement volume that are necessary to arrive at accurate predictions of heat wave propagation in a tokamak plasma.

Finally, a measurement is done on KSTAR shot #18686 to examine the thermal transport near a $m/n = 2/1$ magnetic island. Three ECEI systems are used to observe the inboard side of the magnetic island, the magnetic island itself and the outboard side. It is found that under the conditions of shot #18686 the inboard side system is overexposed and the system observing the magnetic island has a low signal to noise ration for most channels. It is therefore that the second research question of this thesis can not be answered. An analysis of the heat transport is done on the outboard system is done which suggests inwards traveling heat waves from the edge of the plasma. It is suggested that

this could be due to absorption of ECRH energy in the edge of the plasma. To answer the research question it is suggested to do another experiment with a lower fraction of ECRH heating and a more inwards positioning of the ECEI measurement areas.

9 References

[1] S. Kruger. Visualization of the Magnetic Field and Plasma Temperature in D III-D Shot 87009.

[2] M J Choi, J Kim, J.-M Kwon, H K Park, Y In, W Lee, K D Lee, W.-H Ko, J Lee, G S Yun, M Kim, N C Luhmann, Y S Park, Y.-S Na, and B H Park. Interplay between pressure and flow profiles and turbulence near the magnetic island. 2017.

[3] L Bardóczi, T L Rhodes, A Bañón Navarro, C Sung, T A Carter, R J La Haye, G R Mckee, C C Petty, C Chrystal, and F Jenko. Multi-field/-scale interactions of turbulence with neoclassical tearing mode magnetic islands in the DIII-D tokamak. *Citation: Physics of Plasmas*, 24(056106), 2017.

[4] M. Jiang, W.L. Zhong, and Y. Xu. Influence of m / n = 2/1 magnetic islands on perpendicular flows and turbulence in HL-2A Ohmic plasmas. *Nuclear Fusion*, 58, 2018.

[5] GW Spakman, GMD Hogeweij, Rje Jaspers, FC Sc uller, E Westerhof, Je Boom, Igj Classen, E Delabie, C Domier, Ajh Donné, MYu Kantor, A Krämer-Flecken, Y Liang, NC Luhmann Jr, HK Park, O Schmitz, JW Oosterbeek, and the TEXTOR Team. Heat pulse propagation studies around magnetic islands induced by the Dynamic Ergodic Divertor in TEXTOR. *Nucl. Fusion*, 48:115005–10, 2008.

[6] S. Inagaki, N. Tamura, K. Ida, Y. Nagayama, K. Kawahata, S. Sudo, T. Morisaki, and K. Tanaka. Observation of Reduced Heat Transport inside the Magnetic Island O Point in the Large Helical Device. *Phys. Rev. Lett.*, 92(5), 2004.

[7] N J Lopes Cardozo, J C M De Haas, G M D Hogeweij, and W W Xiao. Perturbative transport studies in fusion plasmas. *Control. Fusion*, 37:799–852, 1995.

[8] A Jacchia, P ManticaF De Luca, G Gorini, P Mantica, and F De Luca. Determination of diffusive and nondiffusive transport in modulation experiments in plasmas Determination of diffusive and nondiff usive transport in modulation experiments in plasmas. (3), 1991.

[9] M. van Berkel. *Estimation of heat transport coefficients in fusion plasmas*. PhD thesis, Eindhoven University of Technology, 2015.

[10] I.H. Hutchinson. *Principles of plasma diagnostics*. Cambridge University Press, New York, 2nd edition, 2002.

[11] G. S. Yun, W. Lee, M. J. Choi, J. B. Kim, H. K. Park, C. W. Domier, B. Tobias, T. Liang, X. Kong, N. C. Luhmann, and A. J H Donń. Development of KSTAR ECE imaging system for measurement of temperature fluctuations and edge density fluctuations. In *Review of Scientific Instruments*, 2010.

[12] G. S. Yun, W. Lee, M. J. Choi, J. Lee, M. Kim, J. Leem, Y. Nam, G. H. Choe, H. K. Park, H. Park, D. S. Woo, K. W. Kim, C. W. Domier, N. C. Luhmann, N. Ito, A. Mase, and S. G. Lee. Quasi 3D ECE imaging system for study of MHD instabilities in KSTAR. *Review of Scientific Instruments*, 2014.

[13] T. Kobayashi, K. Ida, and S. Inagaki. Analysis of higher harmonics on bidirectional heat pulse propagation experiment in helical and tokamak plasmas. *Nucl. Fusion*, 57, 2017.